RESEARCH ARTICLE | JANUARY 15 2026

Radial variations in residence time distribution for pipe flows

Etienne Boulais ; Richard D. Braatz

Physics of Fluids 38, 012006 (2026)
https://doi.org/10.1063/5.0307692

Physics of Fluids ARTICLE pubs.aip.org/aip/pof

Radial variations in residence time distribution for pipe flows

Cite as: Phys. Fluids **38**, 012006 (2026); doi: 10.1063/5.0307692
Submitted: 17 October 2025 · Accepted: 14 December 2025 ·
Published Online: 15 January 2026

View Online Export Citation CrossMark

Etienne Boulais and Richard D. Braatz[a)]

AFFILIATIONS

Department of Chemical Engineering, MIT, 77 Massachusetts Ave, Cambridge, Massachusetts 02139, USA

[a)]Author to whom correspondence should be addressed: braatz@mit.edu

ABSTRACT

Suspensions of low-diffusing particles in pipe flows exhibit a difference in age at different radial positions. Particles near the channel walls have higher residence times than the cross-sectional average. We quantify this effect using Monte Carlo simulations and show the existence of two different regimes: a "transitional" regime where delay compounds with channel length and a "far-field" regime where diffusion counterbalances advection. The results presented therein can be used to quantify residence time distributions near the walls of the tube. This effect is important to consider in experiments involving the kinetics of nanometer-scale particles using modern inline analytical tools. This work also provides a radially resolved extension of classical Taylor dispersion results.

I. INTRODUCTION

It is well-known that, in channel flows at high Peclet number, the interaction of lateral diffusion with the parabolic flow profile causes a broadening of concentration clouds. The problem was initially studied by Taylor,[1] who showed that the far-field cross-sectionally averaged concentration cloud tends to a Gaussian profile with an effective diffusivity scaled with Pe^2; this was later refined by Aris,[2] who corrected Taylor's initial estimate for the effective diffusivity. Following this pioneering work, a number of different authors studied the problem. Applications of the model to the measurement of average velocities in pipes have been discussed by Levenspiel and Smith.[3] In a series of papers, Gill and co-workers[4,5] extended the results to cases of different inlet conditions and velocity profiles. Chatwin[6] studied the transient behavior of the concentration cloud in the near-field and its convergence to Taylor's Gaussian profile. In the mid-2000s, some interest in the problem was raised again in the context of microfluidic systems,[7,8] and more recently, experimental work is connecting Taylor dispersion with problems transport in biological systems.[9]

Whereas most work is concerned with the temporal evolution of the concentration of a cloud of tracer, in other words with the distribution of positions of individual particles at fixed times, the problem of residence time distribution asks instead how particles' ages are distributed at a set position in the system. Residence time distribution measurements are common in chemical engineering applications,[10] where techniques for their determination are well-established, and easily applicable to almost any continuous systems. Problems of residence time distributions arise naturally in continuous systems, where measurement equipment is distributed at set positions along a process pipeline, sampling particles of different age at a set position rather than sampling every position in the system at a set instant. The interaction of Taylor dispersion with residence time distributions has been much less studied than the concentration problem. Houseworth[11] gave some analytical scalings, as well as numerical results based on Monte Carlo simulations for the near-field problem. However, the work only considered cross-sectionally averaged quantities and did not report variations of residence times in the radial direction.

Such variations of residence time in the radial direction become important when studying complex kinetics involving colloids or nanoparticles evolving in pipe flow, for example, when probing the self-assembly of lipid nanoparticles,[12] polymeric particles,[13] or other small lipid vesicles.[14] In such a system, because of Taylor dispersion, the relative age of particles at different radial positions in the tube will be quite different. If the studied systems are far from equilibrium, these differences in residence time may translate to significant differences in particle properties (radius, morphology, charge, etc.), depending on the kinetics under study.

In this paper, we show how residence times vary along the cross section in both 2D semi-infinite channels and cylindrical tubes. We show that particles near the wall have higher median residence times, and quantify the effect using Monte Carlo simulations. This effect

becomes important to consider when using noninvasive analytical technologies to characterize particles in pipe flows, in cases where the system's penetration is finite and does not encompass the whole channel. For example, flow dynamic light scattering (DLS) systems[15–17] are used to characterize nanoparticles' size distribution by interrogating a small area near the edge of a channel. Other inline technologies include microscopy systems with finite penetration depth near the tube's surface, optical coherence tomography systems,[18] or spectroscopic systems,[19] to name a few. In such situations, the particles interrogated are not necessarily representative of the whole cross section but instead have a certain delay over the rest, which we quantify in this article. We show that the accumulated delay can be easily of the order of seconds to minutes, depending on the experiment and solute–solvent properties. This effect can be especially significant when studying systems that have kinetics comparable to that delay, for example, in applications related to industrial crystallization or nanoparticle growth.

II. THEORY

Taylor dispersion leads to a lateral broadening of concentration profiles in pipe flows, due to the interaction of advection by the parabolic flow profile and diffusion in the lateral direction. The effect is schematically illustrated in Fig. 1. The probability density P for a particle's position is governed by the advection–diffusion equation

$$\frac{\partial P}{\partial t} = D\nabla^2 P - \vec{u}\cdot\nabla P, \tag{1}$$

where D is the diffusion coefficient and $\vec{u}$ is the velocity field. For flow in a cylindrical channel of circular cross section, the velocity follows the parabolic flow profile $\vec{u}(z) = 2V\left(1-\frac{r^2}{a^2}\right)$, where a is the channel's radius and V is the flow's average velocity. Equation (1) can be nondimensionalized using the scalings

$$\hat{z} = \frac{Dz}{Va^2}, \quad \hat{t} = \frac{Dt}{a^2}, \quad \eta = \frac{r}{a}. \tag{2}$$

In cylindrical coordinates, the equation becomes

$$\frac{\partial P}{\partial \hat{t}} + 2(1-\eta^2)\frac{\partial P}{\partial z} = \frac{1}{\mathrm{Pe}^2}\frac{\partial^2 P}{\partial z^2} + \frac{\partial^2 P}{\partial \eta^2} + \frac{1}{\eta}\frac{\partial P}{\partial \eta} + \frac{1}{\eta^2}\frac{\partial^2 P}{\partial \theta^2}, \tag{3}$$

where $\mathrm{Pe} = \frac{Va}{D}$ is the Peclet number. At high values of the Peclet number, the retrodiffusion term $\frac{1}{\mathrm{Pe}^2}\frac{\partial^2 P}{\partial z^2}$ can be neglected. In addition, if only the variation in the radial distance is of interest, the equation can be averaged over the angular coordinate θ to yield

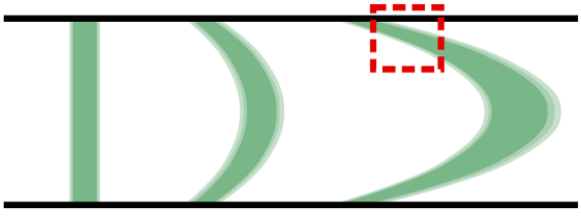

FIG. 1. Schematic of the temporal evolution of a thin plug under the conditions of Taylor dispersion. A noninvasive probing technique may only probe an area near the channel walls, illustrated by the red square. Particles in that area may differ in residence time from particles near the center of the channel.

$$\frac{\partial P^*}{\partial \hat{t}} + 2(1-\eta^2)\frac{\partial P^*}{\partial \hat{z}} = \frac{\partial^2 P^*}{\partial \eta^2} + \frac{1}{\eta}\frac{\partial P^*}{\partial \eta}, \tag{4}$$

where $P^* = \frac{1}{2\pi}\int_0^{2\pi} P d\theta$. Pe is absent from Eq. (4), which means that, in the high Peclet regime, the problem only has to be analyzed once and the results can then be applied to any channel radius, flow rate, or diffusion coefficient through the scalings in Eq. (2).

III. MONTE CARLO SIMULATIONS

In order to study the interplay of residence time distribution and radial position of the particles, we implement the Monte Carlo method described in Ref. 11. The trajectory of individual particles is simulated in a series of discretized steps. Each time step is subdivided into an advection step, where the axial position of the particle is updated

$$\hat{z}_{i+1} = \hat{z}_i + u(\eta)\Delta\hat{t}, \tag{5}$$

and a diffusion step, where the particle is allowed to move along the tube's cross section

$$\eta_{i+1} = f(\eta_i, \Delta\hat{t}), \tag{6}$$

where the new radial position η_{i+1} has to be chosen using an appropriate probability distribution. If small enough timesteps are used, then the diffusion step is approximately decoupled from the advection step. In that case, the probability distribution $\gamma(\eta_{i+1}, \Delta t; \eta_i)$ for the new radial position of the particle η_{i+1}, given the current position η_i, is given by the impulse response of the diffusion equation

$$\frac{\partial \gamma}{\partial t} = \frac{\partial^2 \gamma}{\partial \eta} + \frac{1}{\eta}\frac{\partial \gamma}{\partial \eta}, \tag{7}$$

with boundary condition $\frac{\partial \gamma}{\partial \eta} = 0$ at $\eta = 1$ and initial condition

$$\gamma(\eta_{i+1}, 0; \eta_i) = \frac{1}{\eta_i}\delta(\eta_{i+1} - \eta_i), \tag{8}$$

which corresponds to an infinitely thin ring source located at radial position η_i, where $\delta(x)$ is the Dirac delta function. The solution to this problem is well-known and can be found in handbooks on partial differential equations[20] or in classic treatises on diffusion.[21] For a given time step Δt, we find that

$$\gamma(\eta_{i+1}, \Delta t; \eta_i) = 2\left(1 + \sum_{N=1}^{\infty} \exp\left(-\alpha_N^2 \Delta\hat{t}^2\right)\frac{J_0(\eta_i\alpha_N)\,J_0(\eta_{i+1}\alpha_N)}{J_0^2(\alpha_N)}\right), \tag{9}$$

which can be integrated to yield the cumulative probability function

$$S(\eta_{i+1}, \Delta t; \eta_i) = \eta_{i+1}^2 + 2\eta_{i+1}\sum_{N=1}^{\infty}\left(\frac{\exp(-\alpha_N^2\Delta\hat{t})}{\alpha_N}\frac{J_1(\eta_{i+1}\alpha_N)J_0(\eta_i\alpha_N)}{J_0^2(\alpha_N)}\right), \tag{10}$$

where J_0 and J_1 are Bessel functions of the first kind,[22] and the constants α_N are the positive zeros of the Bessel function J_0. The function S can be numerically inverted to obtain

$$\eta_i = g(S, \eta_{i-1}, \Delta\hat{t}). \tag{11}$$

As a cumulative probability function, S is uniformly distributed between 0 and 1. Given a random number generated from a uniform

distribution between 0 and 1, $g(S, \eta_{i-1}, \Delta\hat{t})$ yields a value for the next radial position, following the correct statistical distribution. To avoid having to invert S at every step, which would be unnecessarily slow, we precompute an interpolant for g on a fine grid covering all possible values of S and η_{i-1}.

We simulate two different initial conditions. The first one is an infinitely thin area source (or plug) with uniform distribution on the cross section at $\hat{z} = 0$, which is done by taking

$$\eta_0 = \sqrt{S}, \tag{12}$$

where S is a random number uniformly distributed between 0 and 1. The square root accounts for the radial distortion of the area element in cylindrical coordinates. We also simulate a uniform flux of particles along the cross section, where more particles appear near the middle of the channel due to the higher flow rate there. Given a random number S, the initial radial position of a particle is then[11]

$$\eta_0 = \sqrt{1 - \sqrt{S}}. \tag{13}$$

The constant flux condition is more representative of a situation where a well-mixed solution is fed into the pipe than the somewhat artificial constant concentration condition. In both cases, the results are qualitatively similar. We present all graphs for both initial conditions in Appendix A.

A. 2D channel

In addition to cylindrical channels, we also analyze the problem for unidirectional flow in a semi-infinite gap between two plates. This problem can come in handy when studying microfluidic channels and chambers which, because of the way they are fabricated, are often correctly modeled as semi-2D systems.[23] The procedure for analyzing the semi-infinite system is exactly the same as for a cylindrical one. In that case, the nondimensional advection–diffusion equation (neglecting longitudinal diffusion) takes the form

$$\frac{\partial P^*}{\partial \hat{t}} + \frac{3}{4}(1 - \hat{y}^2)\frac{\partial P^*}{\partial \hat{z}} = \frac{\partial^2 P^*}{\partial \hat{y}^2}, \tag{14}$$

where $\hat{y}$ is the dimensionless vertical position, with walls situated at $\hat{y} = \pm 1$. The diffusive step in the Monte Carlo algorithm is done the same way as before, this time using the simpler form of the diffusion equation

$$\frac{\partial \gamma}{\partial t} = \frac{\partial^2 \gamma}{\partial \hat{y}^2}, \tag{15}$$

with Green's function[20]

$$\gamma(\hat{y}_{i+1}, \Delta t; \hat{y}_i) = 1 + 2\sum_{N=1}^{\infty} \cos(N\pi\hat{y}_{i+1}) \cos(N\pi\hat{y}_i) \exp(-N^2\pi^2\Delta t) \tag{16}$$

and cumulative probability distribution

$$S(\hat{y}_{i+1}, \Delta t; \hat{y}_i) = \hat{y}_i + \frac{2}{\pi}\sum_{N=1}^{\infty} \frac{1}{N} \sin(N\pi\hat{y}_{i+1}) \cos(N\pi\hat{y}_i) \exp(-N^2\pi^2\Delta t). \tag{17}$$

Initial conditions in the case of the 2D channel geometry are much simpler. For a uniform area source, the initial vertical position $\hat{y}_0$ is simply obtained by generating a uniform random number. For uniform flux, we use the cumulative probability distribution (for the top half-channel)

$$S(\hat{y}_0) = \frac{3}{2}\int_0^{\hat{y}_0} (1 - \xi^2) d\xi, \tag{18}$$

$$S = \frac{3}{2}\left(\hat{y}_0 - \frac{1}{3}\hat{y}_0^3\right). \tag{19}$$

Solving for $\hat{y}_0$ and generating a uniform number between 0 and 1 for S give the proper constant flux distribution in the top half channel.

IV. RESULTS

A. 2D channel geometry

We begin by analyzing the 2D channel geometry, which is somewhat simpler than the cylindrical channel. Results for the cylindrical case are presented in Sec. IV B. We simulate the trajectory for 1×10^6 particles with a time step of $\Delta\hat{t} = 0.001$ and record both their vertical position $\hat{y}$ and their age $\hat{t}$ as they cross set axial distances $\hat{z}$ in the channel. For each axial position, the distribution of $\hat{y}$ and $\hat{t}$ can then be plotted in a 2D histogram, examples of which are given in Fig. 2.

This 2D histogram contains information on both the vertical concentration profile (the sum along the $\hat{t}$ direction is proportional to the time-integrated concentration profile) and the residence time distribution (obtainable by summing along the $\hat{y}$ direction) for different axial distances in the tube. However, this type of plot also contains additional information on the interplay of vertical position, concentration, and residence times, seen through the correlations of the $\hat{t}$ and $\hat{y}$ distributions. In order to visualize some of this interplay, we generate an equivalent of the residence time distribution $E(\hat{t})$ curve that only counts particles whose vertical position $\hat{y}$ is above a certain threshold (corresponding to the particles that are a given distance from the walls of the channel). This is shown in Fig. 3 for a penetration depth of 0.1. We can see that the age of the particles near the wall is, unsurprisingly, slightly higher than those over the entire cross section, which is to be expected due to the lower velocities near the wall.

To compare how this lag evolves with increasing channel length, we compute the median particle age for each distribution, corresponding to the time τ for which

$$\int_0^{\tau} E(\hat{t}) d\hat{t} = \frac{1}{2}. \tag{20}$$

This median time is plotted in Fig. 4(a) for both the entire channel cross section and for the particles for which $|\hat{y}| > 0.9$. We observe that the median age of the particles near the wall initially increases relative to the whole channel, but then stabilizes and grows at the same pace. This effect is illustrated in Fig. 4(b), which plots the difference between the median age of particles near the wall and those in the entire channel. The resulting curve exhibits two distinct regimes, one for low values of $\hat{z}$ where the delay due to the lower average velocity near the wall compounds more or less linearly, and a second one at high $\hat{z}$ where a maximum lag is reached, and the difference in median age between the two distributions remains constant. This region can be interpreted as the one where an equilibrium is reached between the delay caused by lower average velocities near the walls and diffusive

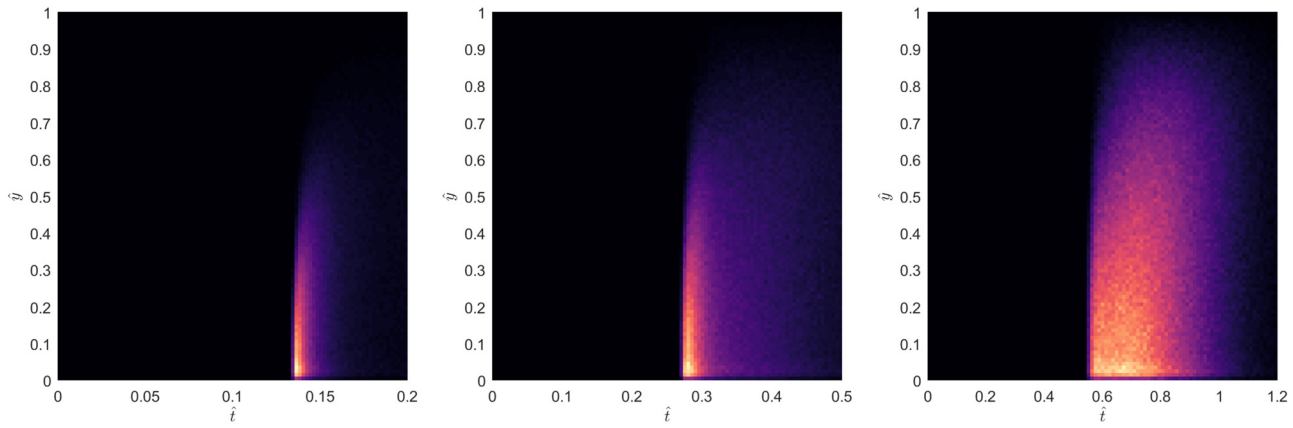

FIG. 2. 2D histogram of vertical position $\hat{y}$ and age $\hat{t}$ of particles crossing different channel lengths $\hat{z}$. 2D channel geometry with constant flux source.

motion exchanging particles between the wall region and the middle of the channel.

As an additional feature of Fig. 4(b), we see that the difference in delay initially "overshoots" the equilibrium value, before slowly settling back down at higher values of $\hat{z}$. We hypothesize that this is due to differences in local equilibration time scales in different regions in the domain, which leads regions near the wall to settle faster than the rest of the channel, initially biasing the delay toward higher values. This effect can also be seen in Fig. 5(b). We next investigate the variation of this delay in the vertical direction, which is illustrated in Fig. 5. Figure 5(a) shows the difference in median residence time between the whole channel and particles for which $\hat{y} > k$ for different values of k ($k = 0$ corresponding to the entire distance between the channel's center and the wall). In each case, the qualitative behavior is the same as observed previously, with lag compounding approximately linearly, then reaching a transition region, then settling on a constant value at higher values of $\hat{z}$. In Fig. 5(b), we compare the difference in median residence time between the whole channel and a thin slice $k_0 \leq \hat{y} < k_1$. We can see that, on average, particles for which $|\hat{y}| > 0.5$ are lagging behind the cross-sectional average, while particles for which $|\hat{y}| < 0.4$ have a smaller median age than the cross-sectional average. The switch between positive and negative lag happens between $0.3 \leq \hat{y} < 0.4$ and $0.4 \leq \hat{y} < 0.5$ curves.

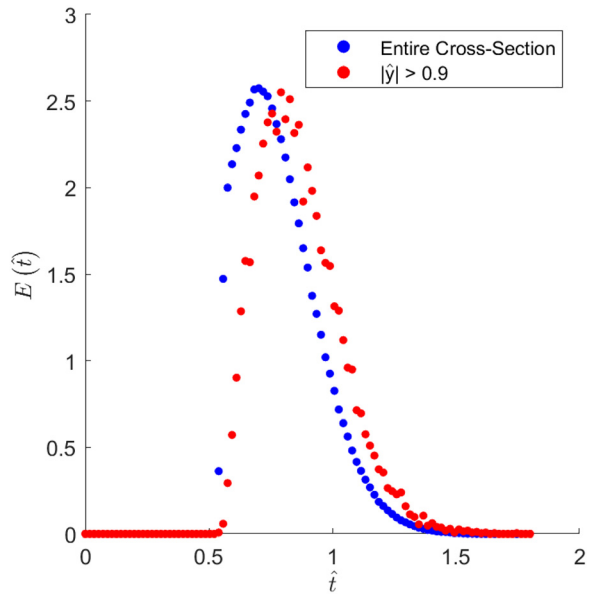

FIG. 3. Residence time distribution $E(\hat{t})$ curve at $\hat{z} = 0.4$ for the entire channel cross section (blue), as well as equivalent curve counting only particles for which $|\hat{y}| > 0.9$ (red). The red curve amounts for a smaller number of particles, but for comparison both curves are normalized to have unit area. 2D channel geometry with constant flux source.

B. Cylindrical channel

We next simulate the evolution of particles in a cylindrical channel. 2D histograms for different channel lengths are shown in Fig. 6. The older age of particles near the wall is particularly visible in this case, with the histogram's shape having a slight diagonal slant. Figure 6 shows count-based histograms, and lower values of η have lower particle counts due to the smaller annular area available at low radius. We plot the effect for different depths, as illustrated in Fig. 7. The curves are qualitatively similar to the rectangular case.

V. PRACTICAL EXAMPLES

The results shown here have practical implications in real systems, and in some cases, there is a risk of committing significant errors if they are not considered. As an example, one of the impetus behind this study was the characterization of experiments in the study of nanoparticle growth using flow dynamic light scattering (DLS)[17] systems. A typical experiment may involve suspension of nanoparticles of radius of about 10 nm. The diffusion coefficient of these nanoparticles can be approximated using the Stokes–Einstein relation

$$D = \frac{k_B T}{6\pi\mu r}, \tag{21}$$

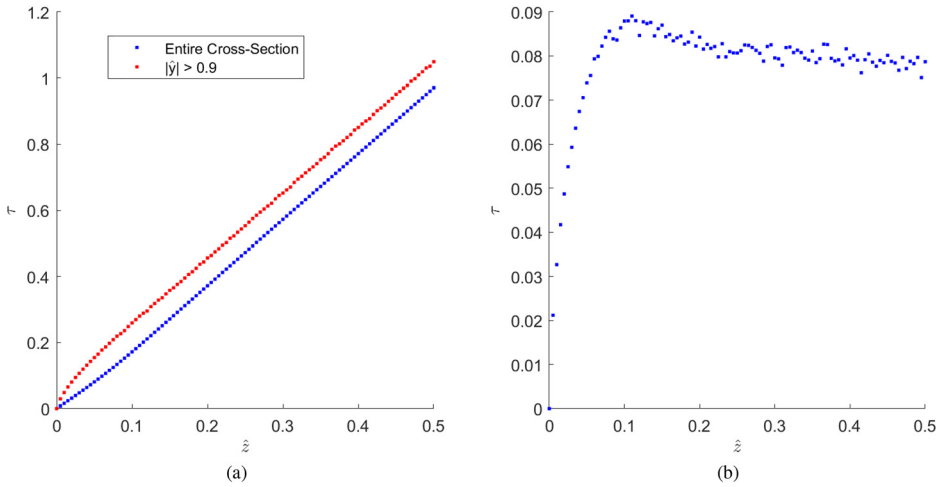

FIG. 4. (a) Median residence time for particles at different axial distances down the channel for entire cross section (blue) and for particles with $|\hat{y}| > 0.9$ (red). (b) Difference in median residence time between both curves. 2D channel geometry with constant flux source.

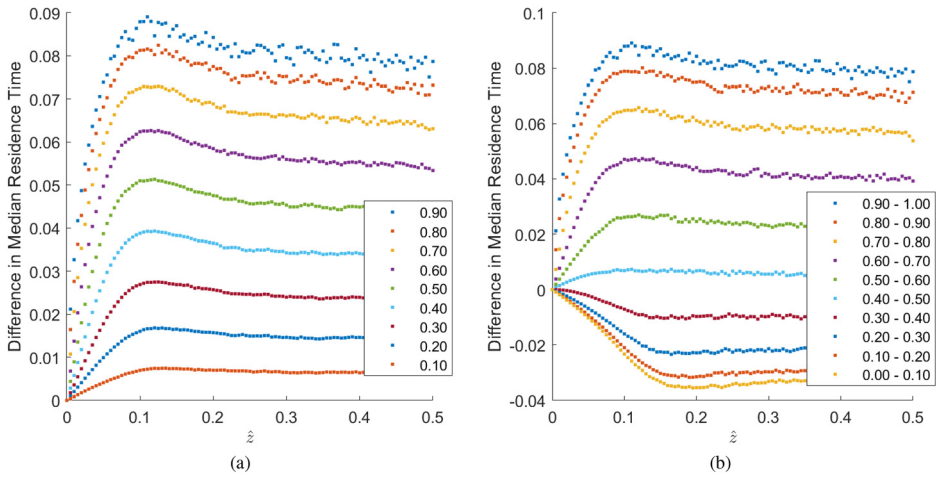

FIG. 5. Difference in dimensionless median time for different penetration depths $|\hat{y}| < k$ (a), as well as for different slices $k_1 \leq |\hat{y}| < k_2$ (b). 2D channel geometry with constant flux source.

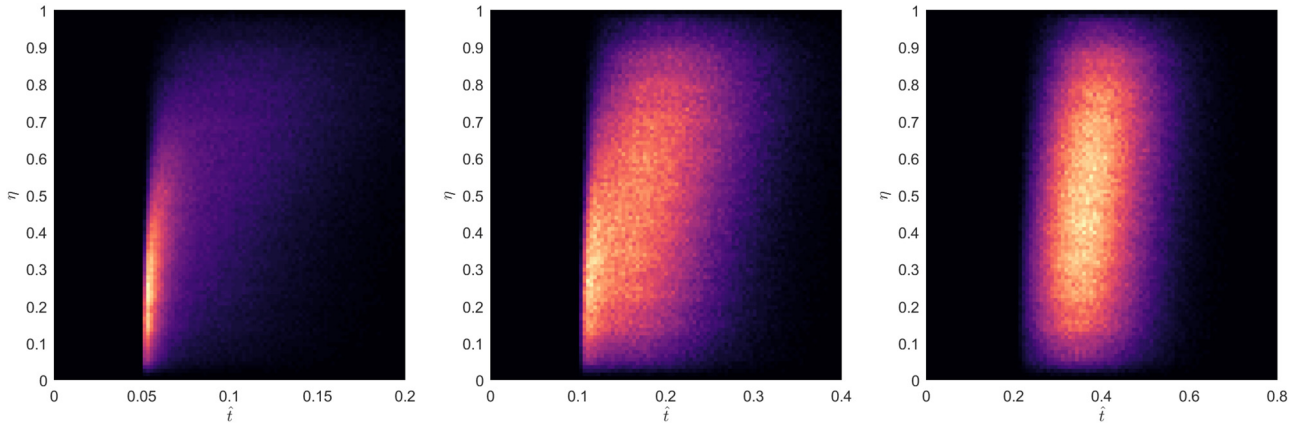

FIG. 6. 2D histograms for cylindrical channel geometries with constant flux source.

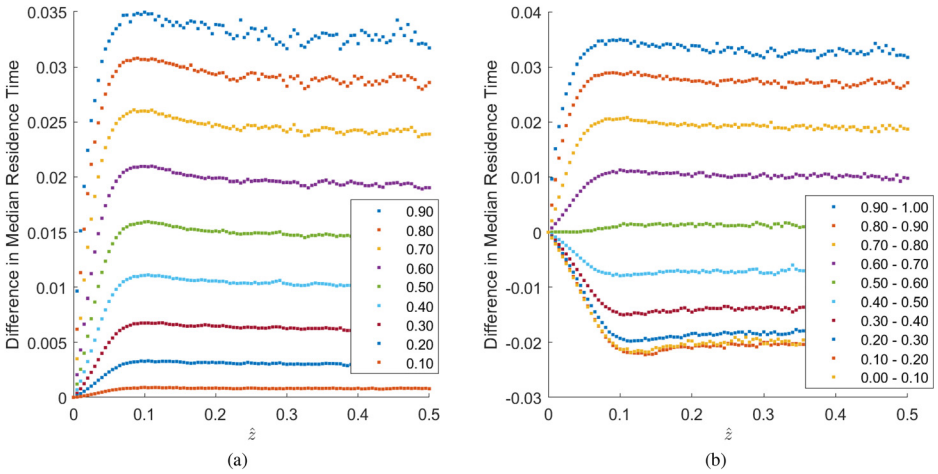

FIG. 7. Median time difference for different penetration depths in a cylindrical channel with constant flux source.

where k_B is Boltzmann's constant, T is the absolute temperature, μ is the solvent's dynamic viscosity, and r is the particle's radius. This yields $D \sim 2 \times 10^{-11}\ \mathrm{m}^2/\mathrm{s}$ at room temperature for a solvent with viscosity comparable to that of water. We have shown in Sec. IV B that the cutoff between the regions of compounding lag and the region of constant additional delay corresponds to roughly $\hat{z} \sim 0.1$ for a cylindrical channel. Plugging our typical values into Eq. (2), this would correspond to a dimensional length of $z_{\text{transition}} = 25\,\mathrm{m}$ for a flow rate of $Q = \pi a^2 V = 100\,\mu\mathrm{l/min}$. If we were to then interrogate particles in the 10% of the channel nearest to the wall, these would have a dimensionless median residence time difference of $\hat{t} \sim 0.033$ with the cross-sectional average [taken from Fig. 7(a)], which for typical tubes with $r \sim 500\,\mu\mathrm{m}$ would here correspond to an enormous dimensional lag of $t \sim 12\,500\,\mathrm{s}$. In this model experiment, if the tube length was shorter than the transition length of 25 m (which it most likely would be), the difference in measured age of the particles would be a more or less linear function of the tubing length used, up to the maximum of $t \sim 12\,500\,\mathrm{s}$ at 25 m. For example, an experiment with 1 m of tubing would see a difference in particles' median age between the wall region and the entire cross section of roughly 500 s. This is important to consider, as it means that the length of tubing used in an experiment can become a variable that significantly affects the measured results.

Further complicating the situation, if the measurement was taken less than 500 s after the start of the experiment, then the difference in the median age of the particles between the region near the edge of the wall and the cross-sectional average would be a transient value that would depend both on channel length and on the moment the measurement was taken (see Appendix B). In experiments that are probing kinetics of nanoparticles using finite penetration depth analytical techniques, Taylor dispersion is going to severely bias the results, such that the particles near the wall are not representative of the entire cross section.

In the numerical example presented above, the Peclet number is $\sim 1.6 \times 10^5$. Peclet numbers of the order of 10^5 to 10^7 for microfluidic systems[24] or up to 10^8 or 10^9 for larger-scale systems[25] are typical, and fall well within the "large Peclet number" ranges necessary for our approximations to hold.

VI. IMPLICATIONS FOR EXPERIMENTAL SYSTEMS

The results presented herein point to further avenues of experimental research. A simple experimental reproduction of our numerical results could be obtained by studying crystallization of a slightly supersaturated solution of a salt in a long tube under flow. Picking a known simple, well-characterized crystallization process would allow a simple correlation of particle size to residence times. Particle size distributions can be measured near the channel walls at different times using a technique such as flow DLS.[17] The measured populations could then be compared to a ground truth obtained by either comparing with known kinetics, or experimentally by running a parallel experiments where the solution is periodically dumped in a vial (thus removing the spatial heterogeneity in populations) and characterized using either traditional DLS or other methods. If different methods are used for characterizing the "near-wall" and cross-sectionally averaged samples, care has to be taken when comparing number-based, volume-based, or intensity-based particle size distributions.[26] In our group's experiments, complex lipid nanoparticles are synthesized using standard impinging jet mixing,[25] and we know that the particles thus formed continue ripening and growing in the tubing, with characteristic timescales of the order of seconds (see Appendix C). Continuous monitoring of such processes is an important problem in modern pharmaceutical applications, and the use of noninvasive systems which sample a small area near the tube's edge will thus have a tendency to sample particles which are older and thus larger than the cross-sectional average. Additionally, if such measurements are made as a way of probing unknown kinetics (which is the case with complex nanoparticle synthesis), not accounting for the spatial variation in residence time distribution will lead to a tendency to overestimate reaction rates, as we are underestimating measured residence times. In complex systems such as lipid nanoparticles where the kinetics are not well-understood, and likely involve population-dependent effects such as particle fusion,[27] the quantitative effect of this inhomogeneity is likely quite complex and could only be studied using complete population balance modeling.[28] Hence, it is important to first study simpler crystallization systems for experimental validation of the work presented here.

VII. OTHER EFFECTS

The results presented here apply to dilute systems, in which the particles are much smaller than the characteristic dimensions of the channel. As the ratio of particle radius to channel dimension increases, and as concentration becomes larger, it may become important to consider interactions between particles and walls, as well as particle–particle interactions. Given the immense breadth of existing nanoparticle flow systems, a complete enumeration of all possible interactions would go beyond the scope of this article. We list here some common ones and point the reader to further reviews on simulations of nanoflows[29] for more details.

Even in the absence of explicit wall forces (for example, electrostatic or van der Waals forces), the flow-induced coupling between the particle and the wall may affect the trajectory of nanoparticles in a number of ways. It is well-known from ideal flow theory (see, for example,[30] Secs. 137 and 138) that flow of a spherical particle near a wall induces a net force on the particle whose direction depends on the direction of movement of the sphere. Variations in drag as a spherical particle move directly toward a wall in Stokes flow are also felt as a net force away from the wall.[31] Small inertial effects can also induce lift forces, which tends to deflect particles away from walls in channel flows.[32] Such lift forces are now known to also arise from symmetry-breaking effects, such as irregular particle shapes or deformable boundaries.[33] Such particle–wall effects could easily be integrated by modifying the lateral diffusion step in our Monte Carlo simulation to account for an additional bias when the particle is near the wall. The addition of a net force away from the wall would have the effect of making the residence time distribution slightly more uniform throughout the channel. In the pure convective system, infinite residence times can be obtained if one gets arbitrarily close to the wall. In regular Taylor dispersion, the interplay of diffusion and advection (even when diffusivity is very small) removes these infinite residence times, as the boundary layer near the wall is diffusively mixed with the interior of the channel. An added bias in diffusion toward the center of the channel would work in this same direction and slightly reduce the net difference in residence times between the wall region and channel interior.

As concentration increases, particle–particle interactions may also need to be considered. These may include fluid mediated interaction between neighboring particles,[34] flocculation,[35] repulsion due to steric stabilization,[36] and eventual Van der Waals or Debye forces[37] between particles. At higher concentrations, effects such as shear-induced migration[38] or shear-induced aggregation[39] may need to be considered. The variety of possible particle–particle effect is very broad, and which ones need to be considered will be heavily problem-dependent. Some of these effects may be integrated into our model by the addition of biasing force, or modified transport coefficients that empirically account for chosen effects. However, in some cases, the presence of complex particle–particle or concentration-dependent effects may break our methodology, in which we are tracking particles one at a time. To account for these more complex effects (for example, particle fusion), fully coupled advection–reaction–diffusion models[40] or population balance models[28] may need to be used. Finally, we have been using simple constant diffusivity computed using the well-known Stokes–Einstein equation. This may break down when studying non-spherical particles, as well as when studying systems where particle size varies a lot over time, and the diffusivity coefficient has to depend on time.

VIII. CONCLUSION

In conclusion, we have shown how residence time distributions of particles vary across the vertical distance in rectangular channel flows, as well as radial distance in cylindrical pipe flows. We have shown that particles near the wall accumulate "lag" up to a certain critical distance, after which diffusion counterbalances advection, and the particles have a constant delay when compared with the cross-sectional average. This effect becomes important in high Peclet number flows, with delays easily adding up to the order of minutes or even hours in typical scenarios. The results presented are of particular importance in experiments probing kinetics (for example, studying the growth mechanisms of nanoparticles) using measurement tools with finite penetration depths, for example, flow DLS systems.

ACKNOWLEDGMENTS

This research is funded by the U.S. Food and Drug Administration under the FDA BAA-22-00123 program, Award No. 75F40122C00200. Etienne Boulais acknowledges funding from the Fond de Recherche du Quebec, Nature et Technologie (FRQNT)

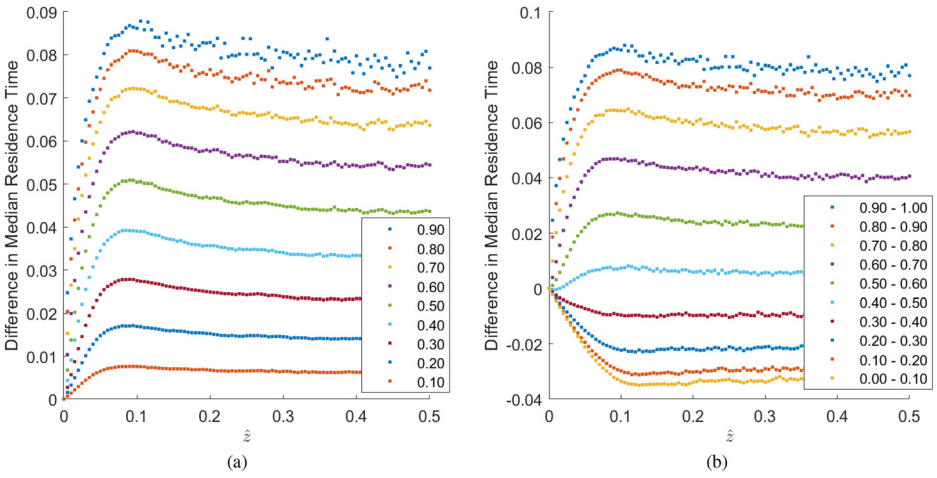

FIG. 8. Difference in dimensionless median time for different penetration depths $|\hat{y}| < k$ (a), as well as for different slices $k_1 \leq |\hat{y}| < k_2$ (b). 2D channel. Initial condition: uniform concentration plug.

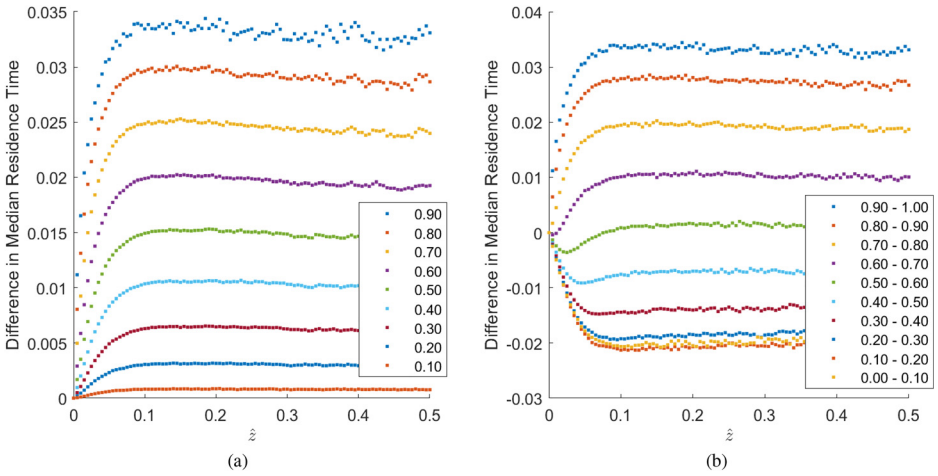

FIG. 9. Difference in dimensionless median time for different penetration depths $|\hat{y}| < k$ (a), as well as for different slices $k_1 \leq |\hat{y}| < k_2$ (b). Cylindrical channel. Initial condition: uniform concentration plug.

Postdoctoral Fellowship Program, as well as the National Science and Engineering Research Council of Canada (NSERC) Postdoctoral Fellowship Program.

AUTHOR DECLARATIONS

Conflict of Interest

The authors have no conflicts to disclose.

Author Contributions

Etienne Boulais: Conceptualization (lead); Formal analysis (lead); Methodology (lead); Visualization (lead); Writing – original draft (lead); Writing – review & editing (equal). **Richard D. Braatz:** Funding acquisition (equal); Project administration (equal); Supervision (equal); Writing – review & editing (equal).

DATA AVAILABILITY

The data that support the findings of this study are available from the corresponding author upon reasonable request.

APPENDIX A: ADDITIONAL RESULTS

The results in the main text were for an initial condition of constant flux through the cross section at $\hat{z} = 0$. Here, we present those same results for an infinitely thin plug of constant concentration at $\hat{z} = 0$. Results are shown for a 2D semi-infinite (Fig. 8) and cylindrical (Fig. 9) channels.

APPENDIX B: TRANSIENT EXAMPLE

Section V provided examples of dimensional delays for particles near a wall in typical experiments. Such delays can easily add up to minutes or hours, once steady state has been achieved. If measurements are taken before that steady state is achieved, the delay will be shorter. Figure 10 shows an example of how that delay evolves for a set position within a cylindrical tube (here, $\hat{z} = 0.02$). For short times, no particle is recorded (when convection has not brought in the first particles), then the difference in median times between the center and edge of the channel compounds until the whole tail has passed. In cases where the delays add up to hours, this means that the difference between the particles near the wall and the cross-sectional average might not just be a function of how far along the tube the measurement apparatus is, but also of how long has elapsed since the experiment started. Considering these effects is important when probing particle kinetics that are of a comparable timescale as the delays induced.

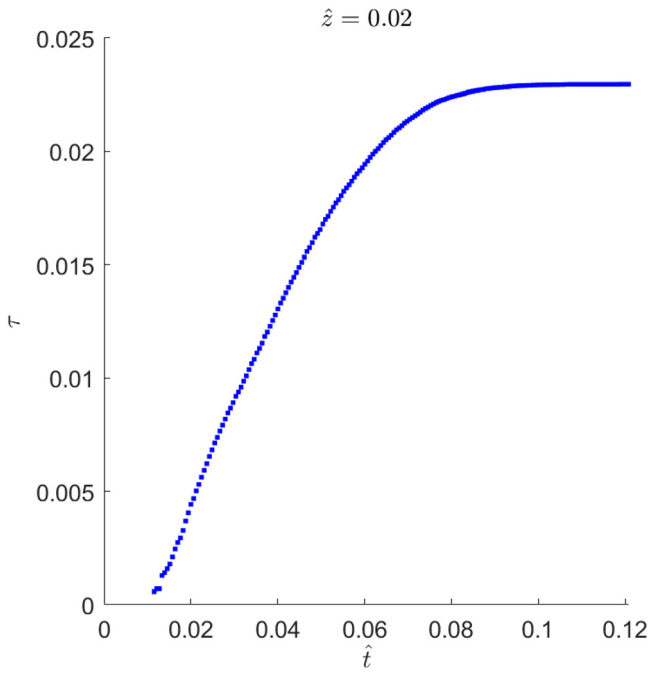

FIG. 10. Difference in residence time between the region near the wall ($\eta > 0.9$) and the cross-sectional average in a cylindrical pipe at $\hat{z} = 0.02$ for short times (constant flux initial condition).

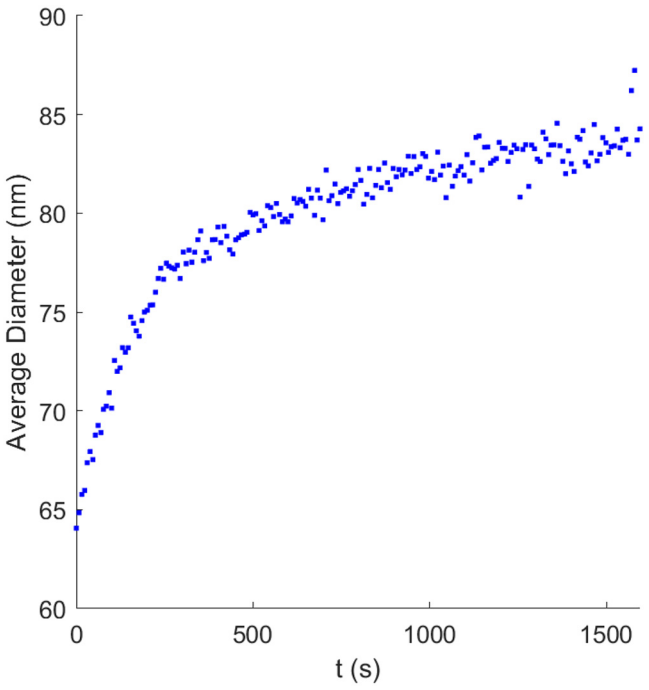

FIG. 11. Evolution of lipid nanoparticle radius in a typical experiment.

APPENDIX C: LIPID NANOPARTICLE EXAMPLE

In Fig. 11, we show the evolution of lipid nanoparticle radius in a typical nanoparticle synthesis experiment over timescales of seconds to minutes. We can observe that the radius changes significantly, growing monotonically over these timescales. Such results, even in the absence of more complete mechanistic models for growth, indicate that higher residence times in such a system are likely to be correlated with higher measured particle radius. We expect similar trends for many nanoparticle synthesis processes.

Drug-free lipid nanoparticles containing ALC-0315 as the ionizable lipid were prepared following the method described in Ref. 41. The lipid concentration in ethanol was 5 mg/ml, and sodium acetate aqueous buffer (pH 5.5) concentration was 100 mM. The lipid nanoparticles were formulated at a total flow rate of 20 ml/min, and the aqueous-to-ethanol flow rate ratio of 3:1. 2 ml of the sample was collected in a glass vial, and the particle size was measured with PhaSR-DLS operated in batch mode. The mean particle size was recorded every 9 s.

REFERENCES

[1]G. I. Taylor, "Dispersion of soluble matter in solvent flowing slowly through a tube," Proc. R. Soc. London, Ser. A **219**(1137), 186–203 (1953).
[2]R. Aris, "On the dispersion of a solute in a fluid flowing through a tube," Proc. R. Soc. London, Ser. A **235**(1200), 67–77 (1956).
[3]O. Levenspiel and W. K. Smith, "Notes on the diffusion-type model for the longitudinal mixing of fluids in flow," Chem. Eng. Sci. **6**(4–5), 227–235 (1957).
[4]V. Ananthakrishnan, W. N. Gill, and A. J. Barduhn, "Laminar dispersion in capillaries: Part I. Mathematical analysis," AlChE J. **11**(6), 1063–1072 (1965).
[5]W. N. Gill, R. Sankarasubramanian, and G. I. Taylor, "Dispersion of a non-uniform slug in time-dependent flow," Proc. R. Soc. London, A **322**(1548), 101–117 (1971).
[6]P. C. Chatwin, "The approach to normality of the concentration distribution of a solute in a solvent flowing along a straight pipe," J. Fluid Mech. **43**(2), 321–352 (1970).
[7]D. A. Beard, "Taylor dispersion of a solute in a microfluidic channel," J. Appl. Phys. **89**(8), 4667–4669 (2001).
[8]A. Ajdari, N. Bontoux, and H. A. Stone, "Hydrodynamic dispersion in shallow microchannels: The effect of cross-sectional shape," Anal. Chem. **78**(2), 387–392 (2006).
[9]A. Vilquin, V. Bertin, P. Soulard, G. Guyard, E. Raphaël, F. Restagno, T. Salez, and J. D. McGraw, "Time dependence of advection-diffusion coupling for nanoparticle ensembles," Phys. Rev. Fluids **6**(6), 064201 (2021).
[10]O. Levenspiel, *Chemical Reaction Engineering*, 3rd ed. (John Wiley & Sons, Hoboken, NJ, 1998).
[11]J. E. Houseworth, "Shear dispersion and residence time for laminar flow in capillary tubes," J. Fluid Mech. **142**, 289–308 (1984).
[12]A. Udepurkar, C. Devos, P. Sagmeister, F. Destro, P. Inguva, S. Ahmadi, E. Boulais, Y. Quan, R. D. Braatz, and A. S. Myerson, "Structure and morphology of lipid nanoparticles for nucleic acid drug delivery: A review," ACS Nano **19**(23), 21206–21242 (2025).
[13]R. C. Hayward and D. J. Pochan, "Tailored assemblies of block copolymers in solution: It is all about the process," Macromolecules **43**(8), 3577–3584 (2010).
[14]J. Leng, S. U. Egelhaaf, and M. E. Cates, "Kinetics of the micelle-to-vesicle transition: Aqueous lecithin-bile salt mixtures," Biophys. J. **85**(3), 1624–1646 (2003).
[15]D. P. Chowdhury, C. M. Sorensen, T. W. Taylor, J. F. Merklin, and T. W. Lester, "Application of photon correlation spectroscopy to flowing Brownian motion systems," Appl. Opt. **23**(22), 4149–4154 (1984).
[16]A. B. Leung, K. I. Suh, and R. R. Ansari, "Particle-size and velocity measurements in flowing conditions using dynamic light scattering," Appl. Opt. **45**(10), 2186–2190 (2006).
[17]R. Besseling, M. Damen, J. Wijgergangs, M. Hermes, G. Wynia, and A. Gerich, "New unique PAT method and instrument for real-time inline size characterization of concentrated, flowing nanosuspensions," Eur. J. Pharm. Sci. **133**, 205–213 (2019).
[18]N. Weiss, T. G. van Leeuwen, and J. Kalkman, "Localized measurement of longitudinal and transverse flow velocities in colloidal suspensions using optical coherence tomography," Phys. Rev. E **88**(4), 042312 (2013).
[19]*Process Analytical Technology: Spectroscopic Tools and Implementation Strategies for the Chemical and Pharmaceutical Industries*, 2nd ed., edited by K. A. Bakeev (John Wiley & Sons, Chichester, UK, 2010).
[20]A. D. Polyanin, *Handbook of Linear Partial Differential Equations for Engineers and Scientists* (Chapman and Hall/CRC, New York, 2001).
[21]J. Crank, *The Mathematics of Diffusion* (Oxford University Press, UK, 1979).
[22]*Handbook of Mathematical Functions: With Formulas, Graphs, and Mathematical Tables*, edited by M. Abramowitz and I. A. Stegun (U.S. National Bureau of Standards, Washington, DC, 1968).
[23]E. Boulais and T. Gervais, "The 2D microfluidics cookbook–Modeling convection and diffusion in plane flow devices," Lab Chip **23**(8), 1967–1980 (2023).
[24]N. M. Belliveau, J. Huft, Paulo, J. C. Lin, S. Chen, Alex K. K. Leung, T. J. Leaver, A. W. Wild, J. B. Lee, Robert J. Taylor, Y. K. Tam *et al.*, "Microfluidic synthesis of highly potent limit-size lipid nanoparticles for in vivo delivery of sirna," Mol. Ther.-Nucleic Acids **1**, e37 (2012).
[25]B. K. Johnson and R. K. Prud'homme, "Chemical processing and micromixing in confined impinging jets," AlChE J. **49**(9), 2264–2282 (2003).
[26]H. G. Merkus, "Particle size, size distributions and shape," in *Particle Size Measurements: Fundamentals, Practice, Quality* (Springer, 2009), pp. 13–42.
[27]A. Kamanzi, Y. Zhang, Y. Gu, F. Liu, R. Berti, B. Wang, F. Saadati, M. A. Ciufolini, J. Kulkarni, P. Cullis *et al.*, "Quantitative visualization of lipid nanoparticle fusion as a function of formulation and process parameters," ACS Nano **18**(28), 18191–18201 (2024).
[28]S. Shin, C. Devos, A. Pradip Udepurkar, P. K. Inguva, A. S. Myerson, and R. D. Braatz, "Mechanistic modeling of lipid nanoparticle (LNP) precipitation via population balance equations (PBEs)," arXiv:2504.10533 (2025).

[29]O. Mahian, L. Kolsi, M. Amani, P. Estellé, G. Ahmadi, C. Kleinstreuer, J. S. Marshall, M. Siavashi, R. A. Taylor, H. Niazmand *et al.*, "Recent advances in modeling and simulation of nanofluid flows—Part I: Fundamentals and theory," Phys. Rep. **790**, 1–48 (2019).
[30]H. Lamb, *Hydrodynamics* (University Press, 1924).
[31]H. Brenner, "The slow motion of a sphere through a viscous fluid towards a plane surface," Chem. Eng. Sci. **16**(3–4), 242–251 (1961).
[32]P. G. Saffman, "The lift on a small sphere in a slow shear flow," J. Fluid Mech. **22**(2), 385–400 (1965).
[33]L. Bureau, G. Coupier, and T. Salez, "Lift at low Reynolds number," Eur. Phys. J. E **46**(11), 111 (2023).
[34]B. Cichocki, B. Ubbo Felderhof, K. Hinsen, E. Wajnryb, and J. Bl/awzdziewicz, "Friction and mobility of many spheres in stokes flow," J. Chem. Phys. **100**(5), 3780–3790 (1994).
[35]P. Meakin, "Formation of fractal clusters and networks by irreversible diffusion-limited aggregation," Phys. Rev. Lett. **51**(13), 1119 (1983).
[36]D. H. Napper, "Steric stabilization," J. Colloid Interface Sci. **58**(2), 390–407 (1977).
[37]J. N. Israelachvili, *Intermolecular and Surface Forces* (Academic Press, 2011).
[38]D. Leighton and A. Acrivos, "The shear-induced migration of particles in concentrated suspensions," J. Fluid Mech. **181**, 415–439 (1987).
[39]V. Oles, "Shear-induced aggregation and breakup of polystyrene latex particles," J. Colloid Interface Sci. **154**(2), 351–358 (1992).
[40]T. M. Squires, R. J. Messinger, and S. R. Manalis, "Making it stick: Convection, reaction and diffusion in surface-based biosensors," Nat. Biotechnol. **26**(4), 417–426 (2008).
[41]C. Devos, A. Udepurkar, P. Sagmeister, A. S. Hodlewsky, J. Chen, A. Hatas, N. Ostrovsky, M. Al-Jazrawe, J. I. Ren, A. Y. Liu *et al.*, "Manufacturing mRNA-loaded lipid nanoparticles with precise size and morphology control," ACS Nano **19**(38), 33991–34002 (2025).